Aerodynamic Analysis of a Winged Sub-Orbital Spaceplane

B. Geiben*, F. Götten*†, M. Havermann*
* Department of Aerospace Engineering, FH Aachen University of Applied Sciences, Aachen, Germany
† School of Engineering, RMIT University, Melbourne, Australia

Abstract

This paper primarily presents an aerodynamic CFD analysis of a winged spaceplane geometry based on the Japanese Space Walker proposal. StarCCM+ was used to calculate aerodynamic coefficients for a typical space flight trajectory including super-, trans- and subsonic Mach numbers and two angles of attack. Since the solution of the RANS equations in such supersonic flight regimes is still computationally expensive, inviscid Euler simulations can principally lead to a significant reduction in computational effort. The impact on accuracy of aerodynamic properties is further analysed by comparing both methods for different flight regimes up to a Mach number of 4.

Keywords

Spaceplane; Sub-Orbital; CFD; RANS; Euler; Supersonic Flow

NOMENCLATURE

Latin Letters

AoA	°	Angle of attack
C_D	[-]	Coefficient of drag
C_L	[-]	Coefficient of lift
C_M	[-]	Coefficient of moment
H	km	Altitude
L/D	[-]	Lift-to-drag ratio
M	[-]	Mach number
M	$\mathrm{kg\,kmol^{-1}}$	Molar mass
p	Pa	Pressure
R	$\mathrm{J\,kg^{-1}\,K^{-1}}$	Specific gas constant
$\mathfrak{R}$	$\mathrm{J\,mol^{-1}\,K^{-1}}$	Universal gas constant
T	K	Temperature
u	$\mathrm{m\,s^{-1}}$	Velocity
y^+	[-]	Normalised wall distance

Greek Letters

α	°	Angle of attack
γ	[-]	Isentropic exponent
μ	Pa s	Dynamic viscosity
ρ	$\mathrm{kg\,m^{-3}}$	Density
$\underline{\underline{\tau}}$	Pa	Stress tensor

Subscripts & Superscripts

$(\,)_\infty$	Freestream condition
$(\,)'$	Fluctuating state
$\bar{(\,)}$	Averaged state

Acronyms & Abbreviations

BC	Boundary condition
CFL	Courant-Friedrichs-Lewy No.
C.O.G.	Centre of gravity
LEO	Low Earth orbit
MAC	Mean aerodynamic chord
N-S	Navier-Stokes
RANS	Reynolds-averaged N-S
S-A	Spalart-Allmaras
STSO	Space Shuttle Orbiter
WISP	Studied Winged Spaceplane

1. INTRODUCTION

The study and development of spaceplane-like vehicles for various applications, ranging from scientific to commercial proposals, has gained popularity in the last decades. While many spaceplanes have been proposed in the last century, very few vehicles have achieved operational status or entered full-size testing. With increasing space commercialisation by private companies and launch providers, the demand for space return vehicles has increased considerably. This is partly based on the imminent exit and lack of competitiveness within government-driven space utilisation. With that and the emergent hope for space tourism as the next step in space commercialisation, spaceplane-like vehicles will play a major role in such ventures. This increases the demand for fast and reliable prototyping and development, which can be provided by means of modern CFD studies.

doi: 10.25967/530170

This paper aims to deliver an aerodynamic CFD analysis on a generic spaceplane geometry, based on one of three openly available Space Walker proposals supported by JAXA [1], Figure 1. This class of sub-orbital vehicles can be used and adapted for various applications, including space tourism and smallsat launch services, concerning altitudes and Mach numbers of up to $120\,\mathrm{km}$ and $M_\infty = 4$, respectively.
A Reynolds-averaged Navier-Stokes (RANS) approach is used in the CFD calculations to study aerodynamic parameters at different flight regimes. Since these calculations are still time-consuming both in preprocessing and processing, an Euler approach is evaluated as a possibly faster alternative. The theoretical foundation suggest good results for reduced computational effort, due to lower resolved meshes, no boundary layer and less equations per iteration to be solved. Nonetheless, the usefulness of the Euler approach has to be studied on a per case basis to compare and compete with the inherently more accurate RANS calculations.

2. CFD SETUP AND METHODOLOGY

2.1. Model Geometry

The WISP geometry is partially based on the publicly available data from the Spacewalker project [1]. In this case the specific geometry is modelled after their smallest spaceplane proposal designed for scientific missions in sub-orbital or LEO configurations, Figure 1. The base geometry has a wingspan of $5.9\,\mathrm{m}$ and an overall length of $9.5\,\mathrm{m}$ and therefore resembles a generic class of currently developed spaceplanes. From here on most design decisions in creating the WISP geometry were chosen to represent the general class of vehicles for an aerodynamic CFD study.

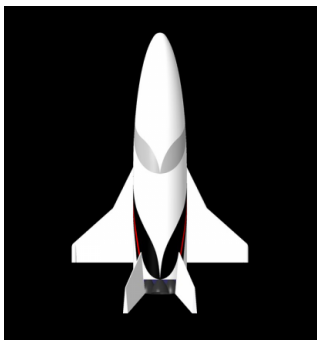

FIG 1. Top down view of the root geometry Spacewalker science mission spaceplane [1].

The entire vehicle, including the delta-wing-like structure and dual rear stabilisers, has been modelled in OpenVSP (see Figures 2a and 2b) and exported as a stereolithography file to be meshed and simulated in StarCCM+ [2]. Within OpenVSP a very fine discretisation has been chosen both to capture all geometric details and deliver a fine baseline model for the CFD meshing [3]. Based on similar projects and the Space Transportation System Orbiter (STSO) configuration, the main wing profile was chosen to be a NACA four-digit series zero lift profile, NACA 0008, with the rear stabiliser profile being a NACA 0012 [4].

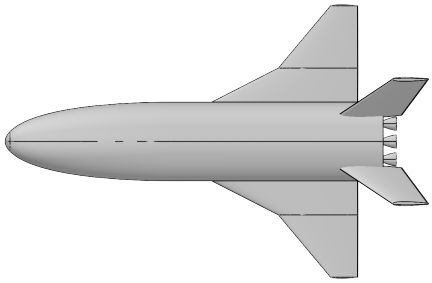

(a) Top down view of 3D model

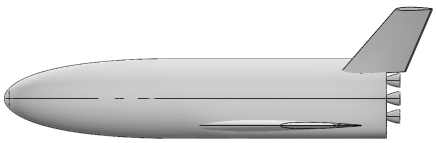

(b) Side view of 3D model

FIG 2. Different model views from OpenVSP software

2.2. Meshing in StarCCM+

The stereolithography file of the Winged Spaceplane (WISP) model, containing the tessellation mesh created by OpenVSP, is imported into StarCCM+ as a surface mesh. In this case, before meshing, some surface repair operations had to be performed in order to present a coherent and closed manifold to the internal StarCCM+ mesher. The specific meshing procedure is dependent on the corresponding CFD simulation and setup. The following meshing setup is performed with a half spherical flow field around the WISP model, Figure 3. The sphere is created with a diameter roughly twenty times the characteristic length of the craft [5] [6]. This results in a half spherical flow field, using the symmetry of the studied problem, with a radius of $100\,\mathrm{m}$. The rear of the Spaceplane is located at the origin of the sphere. Particularly for sonic and supersonic operations, the focus of the simulations, a non-central positioning of the craft can be advantageous. In these cases it allows for a larger downstream flow field, while the upstream flow field should not be affected due the physical nature of supersonic flows.
For this study, three different general meshes were used, all based on the integrated unstructured trimmed cell mesher of StarCCM+ [7]: first, a flow direction orientated high y^+ mesh for RANS simulations; secondly, based on the first mesh, a shock adaptive mesh, refining cells with large density gradients and finally, a lower cell count mesh without a prism layer mesh for the Euler simulations. The Euler simulation workflow is discussed further in section 4.

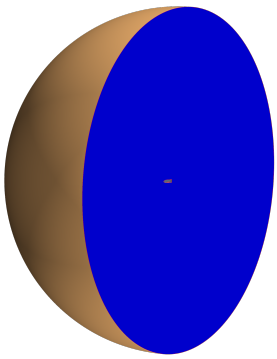

FIG 3. Half spherical flow field with 100 m radius.

In addition to the volume meshes, a surface remesher was used in all cases ensuring full depiction of all geometric features.

2.2.1. RANS Meshing

The RANS CFD meshing pipeline is based on a two step system. The target is to create a coarser base mesh, which is computationally less expensive to then initialise a density gradient refinement function over $\mathcal{O}(10^2)$ iterations. This adaptive mesh refinement is then fed back into the trimmed cell mesher to create a second level mesh. Depending on the quality of the results and the convergence behaviour, a third level mesh, Figure 4, might be created using the same process. The refinement function is created as a field function in StarCCM+ 13.04, which calculates the density gradient of every cell in the mesh normalised to its size. The refinement function assigns a value to every cell, which is then exported into a refinement table that in turn is loaded into the trimmed cell mesher.

```
def CellWidth:
      pow(${Volume}, (1/3))
def DenGrad:
      mag(grad(${Density}))*${CellWidth}
def Refinement:
      ((${WallDistance} < 0.02) ? 0 :
      (${DenGrad} > 0.04) ?
      max(${CellWidth}/2, 0.005) : 0)
```

The base mesh is constructed with multiple surface and volumetric refinements, a full surface remesh and a prism layer mesh. Most surface cells are between 15 mm and 60 mm. The maximum cell size is only limited by the cell size at the boundaries of the flow field and not artificially. Especially curves and other fine geometric features are further refined, which is effectively demonstrated by the span of cell size present on the wing surface. From the largest cells on the upper and lower side of the wing with 30 mm, the feature size is halved three times, over smaller cells (7.5 mm) on the leading edge to the smallest cells on the wing tips at 3.75 mm.
The prism layer mesher discretises the boundary layer region to be described by wall functions with a high y^+ wall treatment. In this case eight to ten

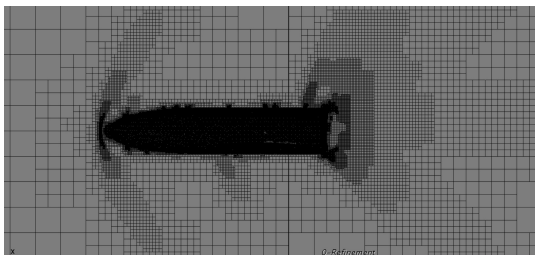

FIG 4. Exemplary level three adaptive mesh.

prism layers are used with a target $y^+ = 30$ first cell height distributed by a “Hyperbolic Tangent” stretching function, as recommended in [6]. Both the total boundary layer thickness and the size of the lowest layer can be approximated beforehand. While the (dynamic) viscosity, density and velocity (as a function of the Mach number and temperature) are variable on all tested configurations, the reference length is constant and has been defined to be the overall vehicle length of 9.5 m. The different flight configurations and related atmospheric values can be obtained from Table 1. After the initial meshing, the adaptive mesh procedure is carried out, which results in a level two adapted mesh with $\sim 2.5 \cdot 10^6$ cells. This can be seen in Figures 5a and 5b. After an additional iteration in the mesh adaption process, a level three adaptive mesh is generated. Such a level three mesh can contain between $\sim 5 \cdot 10^6$ and $\sim 12 \cdot 10^6$ cells, depending on the occurring shocks and density gradients.

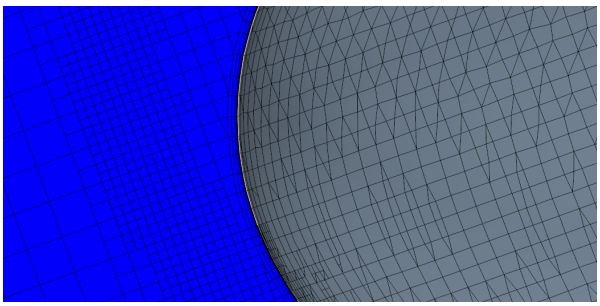

(a) Near mesh view

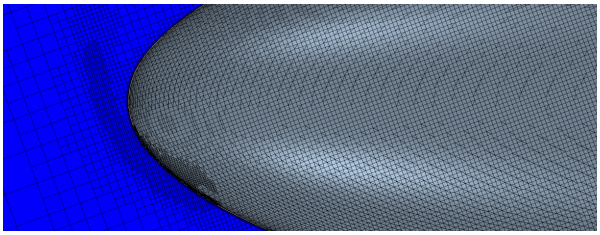

(b) Mid mesh view

FIG 5. Different near-field views of a level two adapted mesh with prism layers and rotated mesh.

2.3. CFD Setup in StarCCM+

From the internal StarCCM+ mesher the simulation files are prepared for both the different flight configurations as well as the two solvers. All of the flight

configurations are derived from a typical descent of a sub-orbital spaceplane, such as our WISP, with a service ceiling of around 100 km [1]. Such a flight profile allows mainly for two types of missions, either a self-powered payload acting as a boosted second stage (resulting in rather small final payload capacities) or a short-term mission using the time in a low gravity and thin atmosphere environment. The time spent in such conditions can range from seconds to a few minutes. The flight configurations tested during the descent of the craft are listed in Table 1, where missing values such as density and velocity can be computed under the assumption of an ideal gas. The atmospheric conditions have been taken from the MSIS-E-90 atmospheric model for mean solar activity [8].

TAB 1. WISP flight configurations for AoA = 20° and AoA = 40°.

M_∞	H [km]	T_∞ [K]	p_∞ [kPa]	μ_∞ [Pa · s]
4	50	250	0.165	$16.15 \cdot 10^{-6}$
3	25	230	3.555	$15.07 \cdot 10^{-6}$
2.5	20	205	5.620	$13.65 \cdot 10^{-6}$
1.3	20	205	5.620	$13.65 \cdot 10^{-6}$
0.8	10	223	26.20	$14.68 \cdot 10^{-6}$
0.3	0	288.15	101.325	$18.12 \cdot 10^{-6}$

Most general settings in the StarCCM+ simulation files are identical for the RANS and Euler calculations, specific solver and physics settings are outlined in subsection 2.3.1 and 4.2, respectively. All simulations were set up for a steady state, using the three-dimensional coupled flow solver with air as an ideal gas. The reference pressure and initial conditions were all set according to the tested flight configuration from Table 1. The magnitude of the velocity is computed as a function of the Mach number and temperature (equation (1)), where $\gamma_{air} = 1.4$ is the isentropic exponent and R is the specific gas constant $R_{air} = \Re M^{-1} = 287.1\,\mathrm{J\,kg^{-1}\,K^{-1}}$ [9]. (In the upper atmosphere the molar mass of air can deviate slightly, however, in the tested regimes this does not have a significant impact [8].)

$$u_\infty = M_\infty \cdot \sqrt{\gamma R T_\infty} \tag{1}$$

The direction of the velocity vector is controlled globally with a rotated coordinate system for AoA = 20° or 40° operations. This global coordinate system is used similarly in any related settings as well as the directional meshing discussed in section 2.2.
Due to the spherical shape of the flow field only three general boundary conditions are in use. First, the "Wall" BC, applied to all surfaces of the WISP geometry; second, a "Symmetry" BC present at the midplane creating the half-spherical flow field. And finally, the shell of the spherical flow field is set to a "Free Stream" BC with the flow direction, Mach number, pressure and temperature defining it [7].

2.3.1. Spalart-Allmaras Turbulence Model

In addition to the physics models that are part of all simulations, a RANS approach with a "High-Reynolds Number Spalart-Allmaras" to model the turbulence has been chosen. The S-A model for external aerodynamics both in incompressible and compressible flow configurations is widely adopted and has been validated extensively for such cases [10]. It is used with a modified high y^+ approach to induce the use of wall functions to model the lower part of the boundary layer. The initial turbulence is specified as a turbulent viscosity ratio of 10.
The convergence behaviour is evaluated under multiple criteria. The weaker criterion is represented by a drop in residuals of three orders of magnitude or more ($\leq 1 \cdot 10^{-3}$), whereas the stronger criterion is evaluated on the convergence of actual aerodynamic coefficients. The lift coefficient and the lift-to-drag ratio are monitored during all simulations to determine the convergence behaviour under consideration of the overall residual behaviour.

3. RESULTS AND DISCUSSION

The major quantitative analyses of this study include lift, drag and moment coefficients plotted over a Mach number sweep, a lift-to-drag ratio analysis, also as a function of the Mach number and multiple lift and drag polars for a landing configuration. For further insight a pressure coefficient analysis is also performed at various configurations. The landing configuration is composed of three additional RANS simulations at M = 0.3 with varying angles of attack [11].
Specific configuration values or definitions, such as the landing Mach number or the definition of the reference area, are chosen in accordance with the Space Shuttle Orbiter (STSO). The descent phase of the STSO is aerodynamically well studied and has delivered a lot of experimental and reliable data for comparisons. Furthermore the STSO is, apart from the classified X37-B [12] and the Soviet Buran, the only generically shaped winged spaceplane with extensive datasets available [11] [13]. Therefore it represents a well-documented comparison point for a preliminary analysis [14].

3.1. Analysis of Aerodynamic Characteristics

Aerodynamic coefficients are computed for optimal compatibility to other studies. The coefficients of lift, drag and momentum are functions of the reference area, which is chosen in accordance with the main comparison point STSO. The moment coefficient is also dependent on a reference length and a working point of the acting moments. For the delta-wing-like structure of the WISP the reference length is calculated as the mean aerodynamic chord (MAC) with 1.814 m. The working point of the acting moments is usually represented by the centre of gravity / mass (C.O.G.) of the craft and is designed to be of minimal distance to the pressure point of the wing or lifting

body. Due to a lack of representative mass distribution data, for this analysis the C.O.G. of the WISP is determined by the centre of volume, computed in OpenVSP. Therefore the momentum coefficient data in this analysis is only qualitative, but can be linearly transformed for future reference, if the true C.O.G. is determined. The reference area is defined to be the entire projected area of the WISP in accordance to the reference area definition of the STSO, which results in $S_{\text{WISP}} = 21.04\,\text{m}^2$ and $S_{\text{STSO}} = 249.9\,\text{m}^2$ [11]. The first RANS analysis concerns the lift and drag behaviour over the studied Mach number range at both angles of attack, Figure 6. First of all, all graphs show the expected general behaviour concerning a peak in value around and after $M = 1$, conforming with the Prandtl-Glauert rule [15]. Therefore the overall qualitative behaviour between the WISP and STSO coincide, with differences in the quantitative data. The STSO produces higher coefficients of lift in all configurations with its advantage ranging between 40 % and 66 %, Figure 6a. This is most easily attributed to the large difference in the wing-to-fuselage ratio. (The wing area is defined as stated previously.) Whereas the STSO has a wing-to-fuselage ratio

$$\left.\frac{S_{\text{Wing}}}{S_{\text{Fuse}}}\right|_{\text{STSO}} \simeq 1.25\,, \tag{2}$$

the WISP only presents a wing-to-fuselage ratio of

$$\left.\frac{S_{\text{Wing}}}{S_{\text{Fuse}}}\right|_{\text{WISP}} = 0.53\,. \tag{3}$$

This effect is more predominant in low Mach number scenarios (see landing configuration, Figure 8a and 8b) and creates a significant difference in lift over the entire Mach number range.
The larger wing area of the STSO, which is greatly based on the much more elongated delta wing structure than present at the WISP, does also create more drag. This specific difference in the wing shape is also clearly demonstrated in Figure 6b when comparing the difference in drag coefficients between AoA = 20° and 40°. With an increase in the angle of attack the elongated wing structure is further orientated against the flow direction.
With these two overlapping effects the lift-to-drag ratio, shown in Figure 7a, presents as expected. The overall behaviour is very similar in all configurations, but deviates most notably in the subsonic regime. For low Mach numbers the pressure distribution is distinctly different than for supersonic Mach numbers, which indicates greater benefits from a larger wing-to-fuselage ratio for subsonic velocities. At 40° ($\lesssim 45°$) angle of attack the lift-to-drag ratio shows nearly Mach independent behaviour at around $L/D \sim 1$. Such static behaviour is also expected, especially in the supersonic range, where the pressure drag (mostly wave drag) is much more dominant than shear related drag forces [9].

The moment coefficient plot, shown in Figure 7b, presents the qualitative pitching moment data gathered in the RANS CFD analysis. The negative pitching moment coefficients, which are important static and dynamic stability parameters, especially during the high-load atmospheric entry / descent phase, follow the generally expected behaviour [16]. By the Prandtl-Glauert rule, particularly at AoA = 20°, the WISP and STSO coincide qualitatively. A quantitative analysis would require reliable data regarding the C.O.G., which might be available in later phases of the development.

3.1.1. Landing Configuration

The study of the landing configuration, Figure 8a, underlines the prior results and closure, where the lift coefficient of the WISP is generally lower and decreases relative to the STSO further with an increasing angle of attack. The same behaviour can be seen when introducing the drag polar in Figure 8b, which indicates again that the increasing angle of attack raises the drag more strongly on the STSO. At very low angles of attack the greater thickness of the STSO's NACA 0012 can delay stall conditions, but also introduces larger pressure drag in comparison to the thinner NACA 0008 used in the WISP design. This part of the overall analysis was not a major study point and the authors recommend further simulations, possibly with a better-suited segregated flow solver and two-equations RANS turbulence model such as k-ω SST [5].
Figures 9 and 10 also supports the results from section 3.1, where the distribution of the pressure coefficient demonstrates the difference in lift creation by over- and underpressure between low subsonic and high supersonic flight. The results are supported by stagnation point C_p values, which are limited to $C_p = 1$ in incompressible flow and $C_p \simeq 1.6$ at $M = 4$.

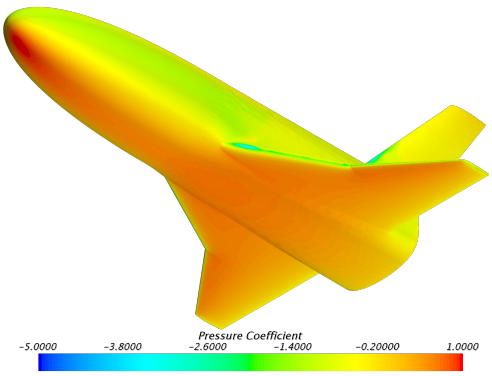

FIG 9. WISP pressure coefficient C_p distribution at M = 0.3; AoA = 40°**.**

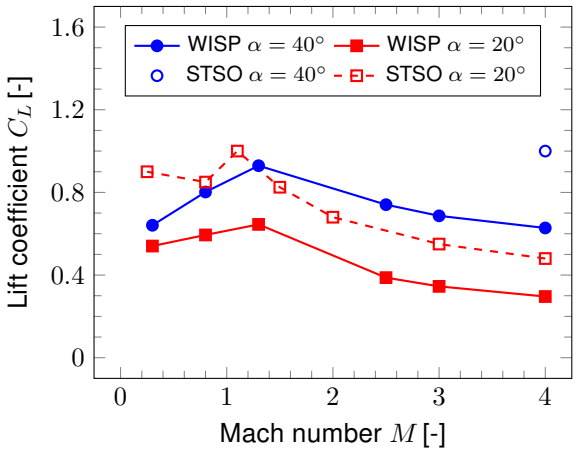

(a) Coefficient of lift

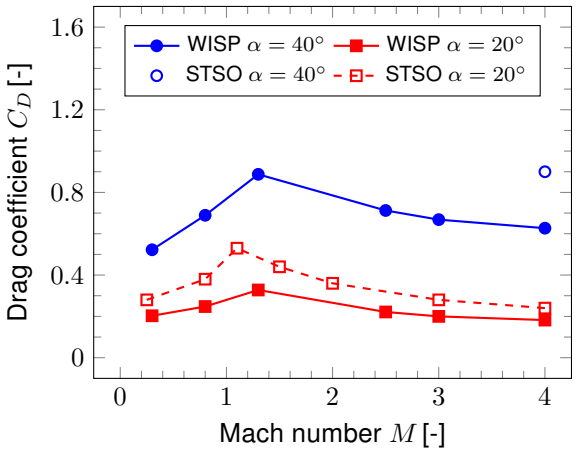

(b) Coefficient of drag

FIG 6. Lift and drag coefficient Mach number sweep.

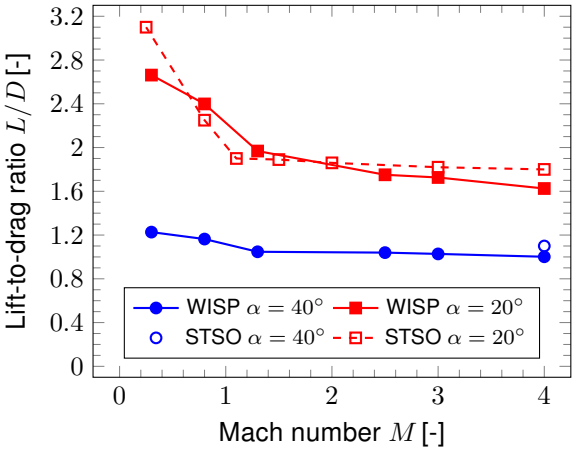

(a) Lift-to-drag ratio

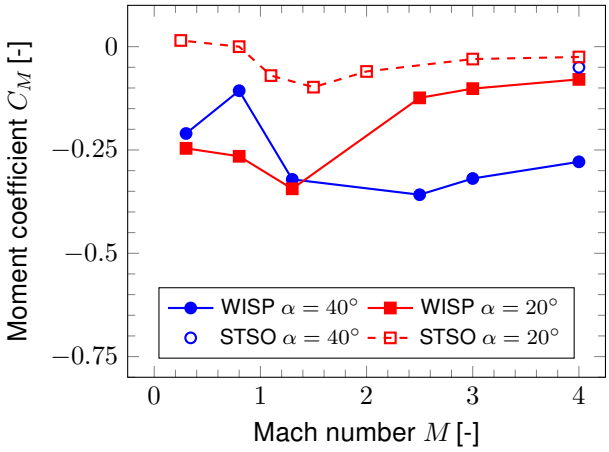

(b) Moment coefficient

FIG 7. Lift-to-drag ratio and moment coefficient Mach number sweep.

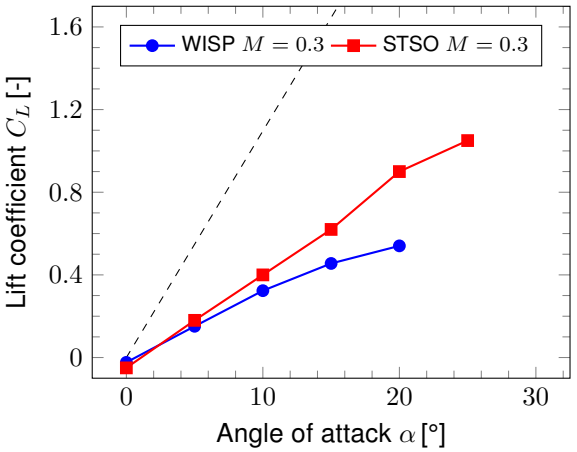

(a) Lift polar, with C_L over α

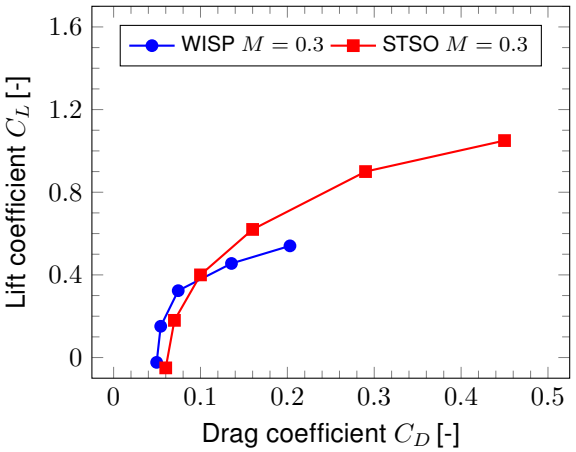

(b) Drag polar, with C_L over C_D

FIG 8. Lift and drag polars for landing configuration at M = 0.3.

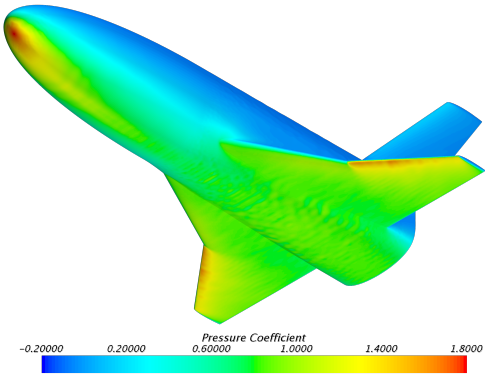

FIG 10. WISP pressure coefficient C_p distribution at M = 4; AoA = 40°**.**

4. FEASIBILITY AND USEFULNESS OF EULER SIMULATIONS

The analysis of supersonic flight configurations is dominated by shock phenomena and the resulting wave drag. This assumption is further validated by the pressure-to-friction drag ratio recorded in the initial RANS CFD simulations. Mostly due to the high angle of attack during most of the descent phase, the pressure drag due to shock wave phenomena far exceeds the viscous drag. This does not hold for lower Mach numbers, especially in the strictly subsonic regime, where the overall drag can be significantly composed of viscous drag. The ratio of forces is further studied in subsection 4.3, in addition to a discussion about the quality of the results and feasibility of Euler simulations.

4.1. Euler Meshing

The mesh used for the Euler simulations is strictly based on the RANS mesh. The only major changes are in a generally coarser mesh with around $50\,\%$ of the RANS base mesh, and the exclusion of any prism layer cells. Due to some numerical instability no further adaptive mesh refinement was used in the Euler simulations. Therefore the mesh sizes in every Euler calculation consistent at $\sim 1.25 \cdot 10^6$ cells.

4.2. Euler Simulations and Differences to RANS

The Euler simulations have been set up on the same basis as the Spalart-Allmaras RANS simulations with a specifically inviscid physics model. In this case no automated grid sequencing is used, mainly due to the lower resolved mesh. Following some numerical stability issues on the sharp trailing edge of the main wing, the CFL number is ramped and limited to 0.5. (The impact on the feasibility of Euler simulations will be discussed later on.)
The RANS momentum equations, here demonstrated with the incompressible case and Einstein notation, can be solved to the point, where from the Reynolds decomposition only the non-linear velocity fluctuation terms persist [17].

$$\rho\frac{\partial \bar{u}_i}{\partial t} + \rho\left(\bar{u}_j\frac{\partial \bar{u}_i}{\partial x_j}\right) = -\frac{\partial \bar{p}}{\partial x_i} + \frac{\partial}{\partial x_j}\left[\mu\left(\frac{\partial \bar{u}_i}{\partial x_j} + \frac{\partial \bar{u}_j}{\partial x_i}\right) - \rho\overline{u_i' u_j'}\right] + \bar{f}_i \tag{4}$$

This term

$$\tau_{ij} = -\overline{\rho u_i' u_j'} = \mu_{\text{turb}}\left(\frac{\partial \bar{u}_i}{\partial x_j} + \frac{\partial \bar{u}_j}{\partial x_i}\right) \tag{5}$$

is also known as the Reynolds stress tensor and is modelled by the according transport equation of a RANS turbulence model such as Spalart-Allmaras or Menter's k-ω SST [18] [17]. Compared to the RANS equations with Spalart-Allmaras turbulence model the Euler equations (Eq. (6)) allow for one equation less to be solved. This reduces the overall computational effort per iteration from six to five equations: three spatial momentum equations, the energy equation (coupled flow solver) and the continuity equation.

$$\rho\frac{\partial \bar{u}_i}{\partial t} + \rho\left(\bar{u}_j\frac{\partial \bar{u}_i}{\partial x_j}\right) = -\frac{\partial \bar{p}}{\partial x_i} + \bar{f}_i \tag{6}$$

Furthermore for compressible calculations additional terms need to be solved, which can further increases the computational effort [19]. However, the effective impact on the computational effort does not necessarily follow such easy rules and will be determined in the subsequent discussion.

4.3. Euler Results and Discussion

The Euler simulations present interesting results concerning both the accuracy and viability. To set a baseline about the accuracy, Figure 11 presents the different drag coefficient results for one Mach number sweep at AoA = 20°. As is expected from the theoretical differences between viscous, inviscid, sub- and supersonic flight, the results deviate the strongest in the subsonic regime. However, it is noteworthy how congruent the curve is during sonic and low supersonic flight considering the much coarser mesh required in addition to the less computationally expensive set of equations to be solved per iteration. In the subsonic Mach number regime the drag force consists mainly of three components, *inviscid* pressure drag, friction drag and pressure drag induced by viscous effects. The latter effect is much more predominant in subsonic flight than in sonic or sonic conditions, where the pressure drag is almost fully produced by supersonic effects, i.e. wave drag [20]. In all flight regimes, the shear stress part of the drag is rather consistent and contributes between $3\,\%$ and $5\,\%$, whereas viscous pressure drag can contribute up to $20\,\%$ to the overall drag at low Mach numbers.
Summarising, this seems to strongly support the effort of reducing the computation time by up to $16\,\%$ per one million cells or up to $79\,\%$ per flight configuration, when studying sonic or supersonic flight.

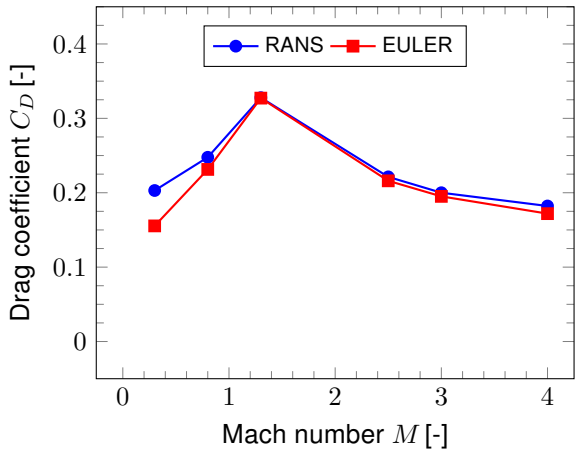

FIG 11. Drag coefficient at AoA 20° for RANS and Euler calculations.

Unfortunately, during the additional Euler simulations some stability and convergence issues occurred, which were later supposedly found to be caused by the geometry and mesh injection into StarCCM+. Therefore in our case, all Euler simulations required more iterations and solver tweaking than expected. Such problems did not occur during any RANS calculations, where presumably the viscous boundary layer dampened many of the geometry induced extreme-condition-cells and resulting stability issues.

5. CONCLUSION

The paper presents an aerodynamic CFD study on a generic spaceplane geometry based on the Spacewalker project. The results show good validity with existing studies and results both from experimental and CFD studies. Especially in the trans- and supersonic regime the Spalart-Allmaras RANS turbulence model delivers good results for a computationally inexpensive one-equation model. In the subsonic regime, mostly demonstrated in the landing configuration angle of attack sweep, a two-equation RANS model might be better suited to further resolve flow separation effects.

Overall, the WISP geometry shows reasonable aerodynamic characteristics and is similar to other flight-tested and in-development spaceplane-like vehicles. It trades some aerodynamic lift for better drag characteristics, especially during high angle of attack phases. Depending on the exact flight path, this could be advantageous to lower the mechanical loads on the craft's structure, but also unfavourable concerning aerothermal loads during the early supersonic return phase. Furthermore, the preliminary study of the pitching moment coefficient presents favourable results for both the static and dynamic stability during all descent phases. (Only the magnitude of the results is preliminary due to the missing data concerning the WISP's centre of mass.)

Regarding the use of Euler simulations for trans- and supersonic flight configurations in spaceplane applications, the authors conclude, that even in times of exponentially increasing computational resources the use of Euler simulations can be time saving if parametric studies are required. However, a very smooth CAD geometry and a proper CFD setup for the Euler calculations is absolutely necessary to gain processing time benefits. Nonetheless, the potential for faster turn-around and rapid prototyping in early development and research stages can be significant.

6. ACKNOWLEDGEMENT

The authors like to express their gratitude to Siemens PLM Software for providing academic licenses of their software StarCCM+.

Contact address:

geiben@fh-aachen.de
havermann@fh-aachen.de

References

[1] Spacewalker Project. https://www.space-walker.co.jp/en. Accessed: 2020-03-13.

[2] OpenVSP Software. http://openvsp.org. Accessed: 2020-08-12.

[3] F. Götten, F. Finger, M. Havermann, C. Braun, M. Marino, and C. Bil. A highly automated method for simulating airfoil characteristics at low reynolds number using a rans - transition approach. 2020. DOI: 10.25967/490026.

[4] J. W. Paulson Jr. *Aerodynamic characteristics of a large aircraft to transport space shuttle orbiter or other external payloads*. National Aeronautics and Space Administration, 1975.

[5] F. Götten, F. Finger, M. Marino, C. Bil, M. Havermann, and C. Braun. *A review of guidelines and best practices for subsonic aerodynamic simulations using RANS CFD*. Asia-Pacific International Symposium on Aerospace Technology 2019, Gold Coast, Australia, December 2019. ISBN: 978-1-925627-40-4.

[6] P. Ewing. Best practices for aerospace aerodynamics. *Star South East Asian Conference*, 2015.

[7] *Simcenter STAR-CCM+ Documentation*. CD-adapco.

[8] M. Kuznetsova, A. Chulaki, N. Papitashvili, et al. MSIS-E-90 Atmosphere Model. https://ccmc.gsfc.nasa.gov/modelweb/models/msis_vitmo.php.

[9] J. D. Anderson. *Modern Compressible Flow*. McGraw-Hill Education, New York, 1990. ISBN: 978-0-072-42443-0.

[10] Siemens CD-adapco. Validation of Star-CCM+ for external aerodynamics in the aerospace industry. http://mdx2.plm.automation.siemens.com/sites/default/files/Presentation/CD-adapco_AeroValidation_v7.pdf. Accessed: 2020-08-14.

[11] Claus Weiland. *Aerodynamic data of space vehicles*. Springer, Heidelberg, 2014. ISBN: 978-3-642-54167-4.

[12] John Pienkowski et al. Analysis of the aerodynamic orbital transfer capabilities of the x-37 space maneuvering vehicle. In *41st Aerospace Sciences Meeting and Exhibit*. American Institute of Aeronautics and Astronautics, 1 2003. DOI: 10.2514/6.2003-908.

[13] *N.N. Aerodynamic Design Data Book - Orbiter Vehicle STS-1*. Rockwell International, 1980.

[14] K. W. Iliff and M. F. Shafer. *Space Shuttle Hypersonic Aerodynamic and Aerothermodynamic Flight Research and the Comparison to Ground Test Results*. NASA Dryden Flight Research Facility, 1993. NASA Technical Memorandum 4499.

[15] Fritz Dubs. *Hochgeschwindigkeits-Aerodynamik*. Birkhäuser, 1975. ISBN: 3764307145.

[16] Mark Drela. *Flight Vehicle Aerodynamics*. The MIT Press, 02 2014. ISBN: 978-0-262-52644-9.

[17] W. K. George. *Lectures in Turbulence for the 21st Century*. Imperial College of London, 2013.

[18] H. Tennekes. *A First Course in Turbulence*. The MIT Press, Cambridge, Massachusetts, 1992. ISBN: 978-0-262-20019-6.

[19] J. Ferziger. *Numerische Stroemungsmechanik*. Springer, Berlin Heidelberg, 2008. ISBN: 978-3-540-67586-0.

[20] F. Janser, M. Havermann, B. Hoeveler, and C. Hertz. *Inkompressible Profil- und Tragfluegelaerodynamik*. Verlagshaus Mainz GmbH, Aachen, 2016. ISBN: 978-38107-0261-6.